Journal of Inorganic and General Chemistry

ZAAC

Zeitschrift für anorganische und allgemeine Chemie

www.zaac.wiley-vch.de

RESEARCH ARTICLE

Check for updates

Continuous Microreactor-Based Synthesis of SnO$_2$ Nanoparticles for Sensor Applications

Christina Odenwald,[a] Lucas Niedner,[a] Robert Haberkorn,[a] Tilman Sauerwald,[b, c] Oliver Brieger,[c] Mike Nadig,[a] and Guido Kickelbick*[a, d]

Dedicated to Prof. Dr. Dr. h. c. Michael Veith on the occasion of his 80th birthday.

Tin oxide nanoparticles are well-established materials with a wide range of applications, including optoelectronic devices and solid-state gas sensors. Conventional synthesis methods of these systems are often based on batch processes. In this study, we compare batch and continuous synthesis methods for tin dioxide nanoparticles using precipitation and sol-gel processes. For the continuous processes we applied the so called microjet reactor method. The nanoparticles were characterized by TEM, elemental analysis and XRD and exhibited particle sizes of 1.7–3.0 nm and crystallite sizes of 1.7–2.3 nm, consisting of tetragonal (*P*4$_2$/*mnm*) and orthorhombic (*Pbcn*) phases. We have evaluated different post-synthesis purification methods to remove impurities such as chlorides and carbon-hydrogen species. Each purification method exhibited unique advantages and side effects, providing insight into selecting the most appropriate method for specific applications. We also demonstrated the potential of these SnO$_2$ nanoparticles as ethanol gas sensing materials and compared their performance with a commercial sensor.

Introduction

Tin dioxide (SnO$_2$) is a transparent semiconductor known for its excellent optical, electronic and chemical properties that make it valuable for a variety of technologies such as gas sensors,[1–2] solar cells,[3] catalysts[4] and anode materials for Li-ion batteries.[5–6] Although it is the most extensively studied prototype oxide-based gas sensor, ongoing research in this area is driven by the quest to develop sensors with improved specificity and sensitivity.[7–8] The literature describes in detail batch processes for the production of SnO$_2$ materials and nanoparticles and investigates their influence on material properties. Some examples are hydrothermal or solvothermal preparation methods,[9–10] microwave syntheses,[11–12] sonochemical methods,[13] polyol syntheses,[14] ball milling reactions,[15] molten salt methods,[16] (non-aqueous) sol-gel,[17–19] precipitation[20–22] and microemulsion[23–24] proceedings. In many cases the precursor chemistry plays a major role for the final properties of the materials. Mainly tin(II) or tin(IV) chloride salts or elemental tin are preferred because they are easy to handle and inexpensive.[25] For sol-gel reactions different tin alkoxides (e.g. Sn(O^{t}Bu)$_4$, [Sn(O^{i}Pr)$_4$ · HO^{i}Pr]$_2$ or [Sn(OEt)$_4$]$_n$) have been used or compounds with hydrolyzable Sn-alkyne bonds, such as RSn(C≡CR')$_3$ or (RC≡C)$_3$Sn(spacer)Sn(C≡CR)$_3$.[26–29] Also studies by Veith *et al.* have shown that molecular tin alkoxide compounds serve as excellent starting materials for various tin-based materials, mainly in CVD or wet chemical batch processes.[30–32] Continuous preparation methods for SnO$_2$ materials are less frequently reported, but offer significant advantages in terms of reproducibility, scalability and process control.[33–35] Typical continuous synthesis methods for nanostructured SnO$_2$, SnO$_2$ composites or doped SnO$_2$ include hydrothermal[36–39] and solvothermal processes,[40] flame synthesis[41–42]/spray synthesis,[43] pyrolysis reactions and vapor growth methods.[44] Less common methods are microfluidic systems and flow syntheses.[45–47] In the past, we introduced the microjet reactor method for the production of various metal oxides, which enables the production of large quantities of materials with consistent quality.[48–51] Wet chemical synthesis methods offer the advantage of producing less aggregated particles with active surface groups.[52] Depending on the precursors used, various impurities are introduced into the products. Chloride can have a negative effect on the surface and the electrical properties of SnO$_2$. Literature reports describe changes in particle agglomeration and stabilization,[53] reduced gas sensor

[a] C. Odenwald, L. Niedner, R. Haberkorn, M. Nadig, G. Kickelbick
   Inorganic Solid State Chemistry, Saarland University, Campus Building C4 $_1$, 66123 Saarbrücken, Germany
   E-mail: guido.kickelbick@uni-saarland.de
[b] T. Sauerwald
   Department for Sensory Analytics and Technology, Fraunhofer-Institute for Process Engineering and Packaging, Giggenhauser Str. 35, 85354 Freising, Germany
[c] T. Sauerwald, O. Brieger
   Department of Systems Engineering, Saarland University, Building A5 $_1$, 66123 Saarbrücken, Germany
[d] G. Kickelbick
   Saarene-Saarland Center for Energy Materials and Sustainability, 66123 Saarbrücken, Germany

performance,[54] adverse effects on sintering temperature[53] and inhibition of catalytic processes[55] due to chloride impurities. Hence, it is important to investigate the impurities incorporated by the synthesis, their influence on particle properties and their removal after particle formation.[38,56–59]

In the present study, we compared a straightforward batch synthesis of SnO_2 nanoparticles using $SnCl_4$ and $Sn(O^tBu)_4$ as precursors with the continuous synthesis. The influence of the precursors and reaction conditions on the particle morphology, crystallinity and composition was systematically studied. For a selected particle sample from the continuous preparation process, we studied its suitability as gas sensor materials. Since the purification method is important for many applications, we also investigated its influence on particle composition and annealing behavior.

Results and Discussion

Comparison of Different SnO_2 Preparation Routes

SnO_2 nanoparticles were prepared in a batch procedure (magnetically stirred beaker synthesis) and by a continuous synthesis (microreactor). Furthermore, two different precursors and reaction types were compared, namely a precipitation reaction, starting from aqueous $SnCl_4 \cdot 5\,H_2O$ and NH_3 solutions and a sol-gel reaction, starting from $Sn(O^tBu)_4$. The samples from precipitation reaction are labeled as: $Prec:B_{ap}$ or $Prec:M_{ap}$, according to the applied synthesis method (beaker or microreactor). For sol-gel samples analogous abbreviations ($Sol:B_{ap}$ and $Sol:M_{ap}$) were chosen. The subscript indicates the post-treatment, whereby ap stands for "as prepared". All FT-IR

spectra (Figure 1 A) show a characteristic, broad vibration band at $500\,cm^{-1}$ from bulk metal-oxygen vibration with a shoulder at $655\,cm^{-1}$. Absorption bands in the range of 830–$1350\,cm^{-1}$ can be attributed to the bending modes of different types of surface OH-groups.[60–62] The vibration band at $1042\,cm^{-1}$ from sol-gel samples might also originate from t-butoxy groups.[63] The absorption peak at ca. $1635\,cm^{-1}$ is assigned to the deformation mode of water,[60,62] whereas the peak at $1450\,cm^{-1}$ originates from a derivate of ammonia, because it only appears in precipitation samples.[53] The broad vibrational band at 2560 to $3660\,cm^{-1}$ can be associated with the stretching vibration of O—H bonds due to hydroxide groups and adsorbed water.[60,64]

The XRD scans of the powder samples (Figure 1 B) were analyzed by Rietveld refinement to determine the phase composition, as well as the crystallite size and lattice parameters. The main phase in all samples could be identified as tetragonal SnO_2 (rutile type, $P4_2/mnm$, ICSD collection code 647465),[65] whereas a refinement with solely this phase resulted in an inadequate fit in some regions (e.g. at $2\theta = 24$–$36°$ or $2\theta = 56$–$68°$). From literature also two orthorhombic high-pressure phases HP1 ($CaCl_2$-type, $Pnnm$) and HP2 (α-PbO_2, $Pbcn$) are known for SnO_2.[66–69] The $Pnnm$ structure is closely related to the tetragonal phase and cannot be clearly distinguished in powder XRD, especially in the case of nanocrystalline materials.[70] The proportion of this phase is therefore attributed to the tetragonal phase and is not documented separately. Implementing the phase HP2 ($Pbcn$, structure data adapted from Jensen $et\,al.$[70]) into the Rietveld refinement improves the overall fit. E.g. for the sample $Prec:M_{ap}$ the goodness of fit (GOF) value decreases from 1.48 to 1.10 if a $Pbcn$ phase is added. The misfit in the region $2\theta = 24$–$36°$ is suspended by the (111) reflection of the α-PbO_2 phase and similarly, the reflections of
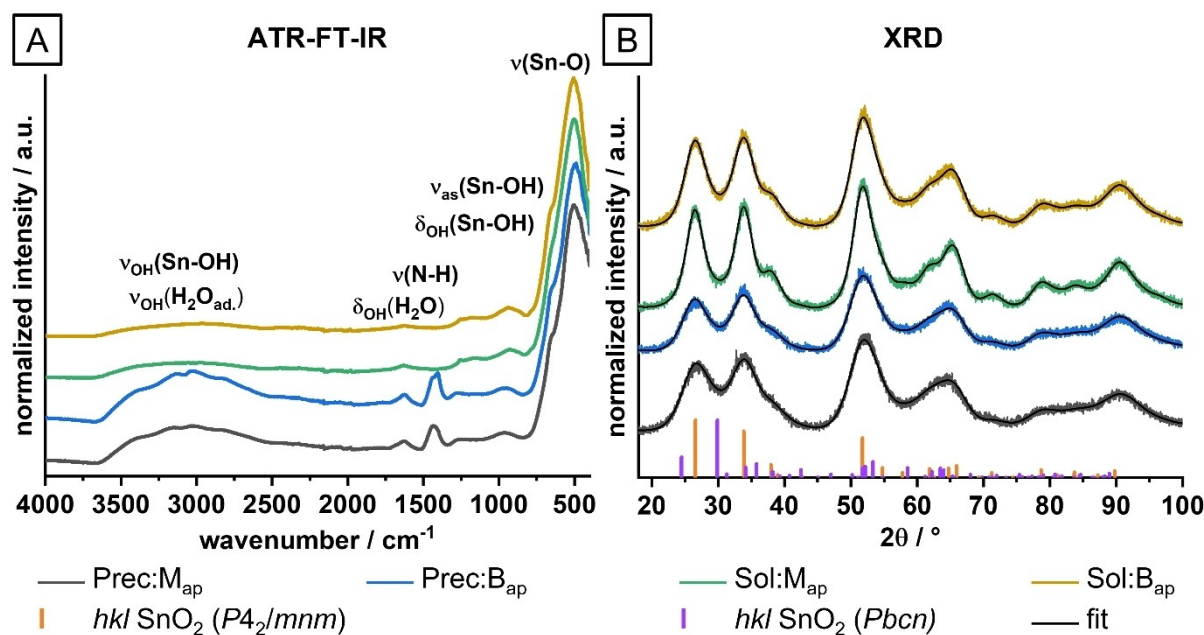

Figure 1. (A) ATR-FT-IR spectra and **(B)** XRD patterns of the samples prepared by different precursors and synthesis methods arranged in a staggered manner. All samples were used "as prepared", which means without any further purification.

the α-PbO_2 SnO_2 phase improve the fit in the $2\theta = 56$–$68°$ region (Figure S4). Although a slight misfit remains, it is still smaller than that observed when using a model of a multi-fractioned rutile-type SnO_2 phase. It is also likely that an amorphous phase is present, which cannot be fully isolated from the $Pbcn$ phase due to the severe peak broadening.

For the rutile-type phase, cell parameters of $a = 4.761(1)$ Å, $c = 3.187(1)$ Å and for the α-PbO_2-type phase cell parameters of $a = 4.718(2)$ Å, $b = 5.723(2)$ Å and $c = 5.258$ (2) Å were determined at room temperature.

The phase weight fractions of the different phases for all samples were refined by keeping the cell parameters constant. Crystallite sizes (main phase) between 1.7 and 2.3 nm were calculated, whereby the crystallites for sol-gel derived materials are slightly larger than those from the precipitation processes (Table 1). In addition to the signals of SnO_2 an extra reflection at $2\theta = 32.7°$ (Figure S4) is visible in some samples, which could be assigned to NH_4Cl[71] the byproduct of the precipitation reaction.

TEM images (Figure 2 A) reveal particles sizes between 2–3 nm, which are comparable to values obtained in the literature for batch synthesis procedures.[21,72] High-resolution TEM and diffraction images of the Sol:B_{ap} sample (Figure S5) show the lattice fringes and confirm that crystalline particles mainly in the tetragonal cassiterite phase were obtained. Some grains were found to consist of more than one crystallite, which explains the slightly higher values of grain sizes measured by TEM compared to the crystallite sizes from XRD.

TGA curves (Figure 2 B) display significant mass differences between precipitation and sol-gel samples. The mass loss of precipitation samples is between 15 % (Prec:M_{ap}) and 18 % (Prec:B_{ap}), for sol-gel samples the values are between 7 % (Sol:M_{ap}) and 8 % (Sol:B_{ap}). The type of leaving groups causing the different losses are determined in the second part of the article.

Comparing the samples produced by different methods (beaker and microreactor), no strong influences on the mass losses are observed, leading to the conclusion that the particles have similar surface areas and groups. The chemical composition of the particles was studied with elemental analysis and EDX (Table 2).

The particles from precipitation involve 2.0–2.7 wt% nitrogen and 4.6–6.2 wt% chlorine, introduced by the educts. In the

Table 1. Crystallite sizes and phase weight fractions of the rutile ($P4_2/mnm$) and orthorhombic ($Pbcn$) phases obtained by XRD and particles sizes measured from TEM images.

	crystallite size ($P4_2/mnm$)/nm	phase fraction $P4_2/mnm$/wt %	phase fraction $Pbcn$/wt %	particle size/nm
Prec:B_{ap}	1.82(3)	83	17	2.7(4)
Prec:M_{ap}	1.67(3)	72	28	≈ 1.7[a]
Sol:B_{ap}	2.09(3)	80	20	3.0(8)
Sol:M_{ap}	2.25(3)	86	14	2.9(6)

[a] The average size was determined by measuring only 40 individual particle diameters because the particles were very small and therefore highly agglomerated.
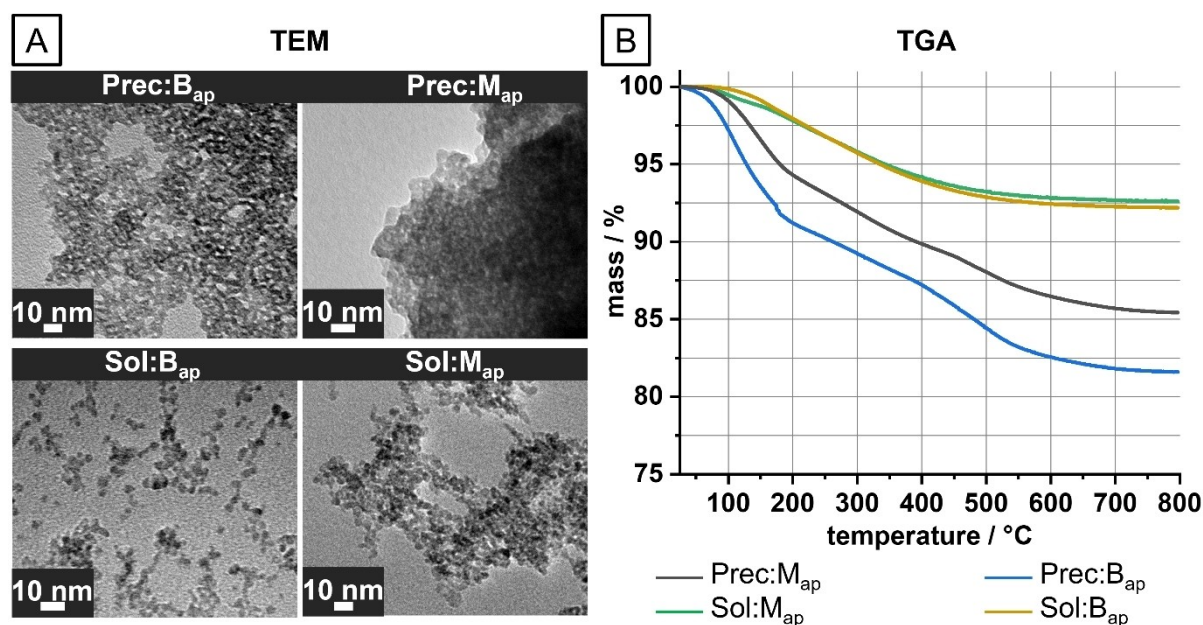

Figure 2. (A) TEM images and (B) TGA curves of the SnO_2 samples prepared by different methods and precursors.

Table 2. Chemical composition of the as prepared SnO_2 particles obtained from elemental analysis (C and N) and EDX (Sn and Cl). n. d.: not detectable.

	C/wt%	N/wt%	Sn/wt%	Cl/wt%	Cl:Sn atomic ratio
Prec:B_{ap}	n. d.	2.7	74.3	6.2	0.3
Prec:M_{ap}	0.2	2.0	74.7	4.6	0.2
Sol:B_{ap}	0.4	n. d.	78.7	0.5	0.02
Sol:M_{ap}	0.4	n. d.	79.6	0.6	0.02

sol-gel samples the nitrogen content was below the detection limit, and a slightly increased amount of carbon was recorded. Surprisingly, the sol-gel samples also contain a small amount of chlorine (≈ 0.5 wt%), which must originate from the synthesis of the sol-gel precursor.
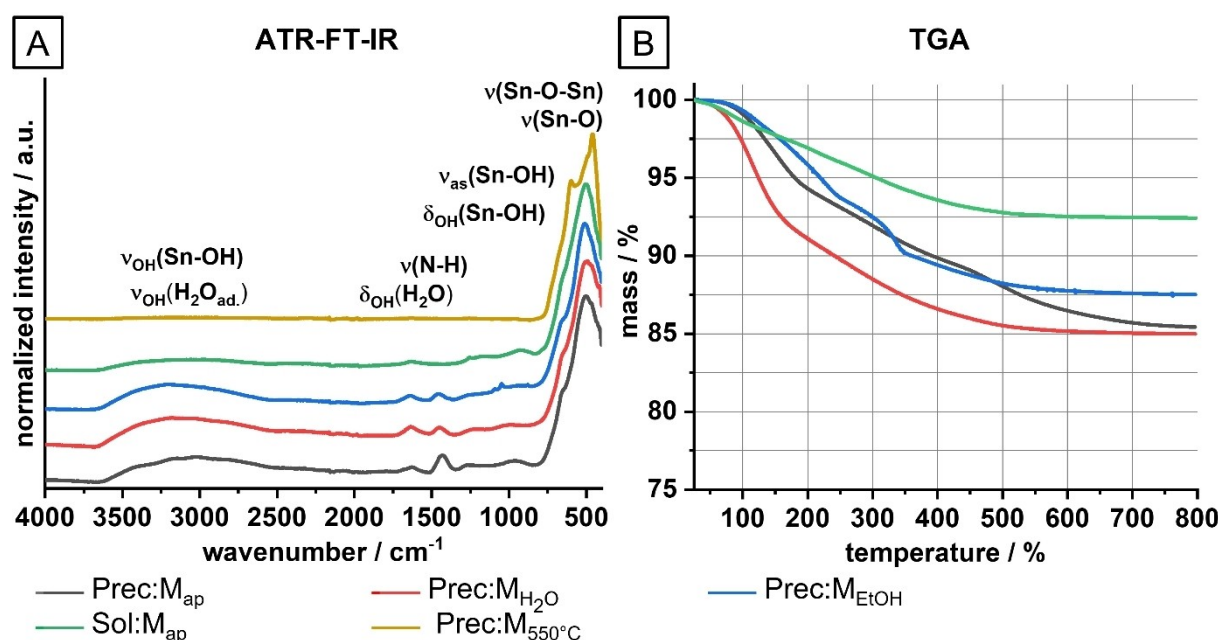
According to the presented results, both preparation methods (beaker and continuous microreactor) yielded nanocrystalline SnO_2 particles (2–3 nm in size) with $P4_2/mnm$ as the main phase. The results show that the chosen precipitation and sol-gel routes are very robust and a transfer from batch to continuous route is easily possible. The small sizes are in demand for many applications, e.g. as an additive in the photoactive layer of polymer solar cells or in combination with polyvinyl alcohol to produce transparent and flexible thin films that can be used as humidity sensors.[73–74] Although the continuous reaction produces particles with similar properties to the batch process, this method offers advantages for technical or industrial scales. For example, the continuous production rate is easier to integrate into a workflow, including the subsequent cleaning and further processing of the particles. In addition, the smaller volume of the microreactor enables faster response times compared to a stirred batch reactor. This means that in the event of problems, corrective action can be taken more quickly, minimizing the impact on the overall solution.

Purification Methods and Influence of Chlorine on the Tempering Behavior

Given the relevance of impurities on the properties of SnO_2 and thus for their applications,[53–55] we applied different purification processes on the continuously produced nanoparticles. The feasibility of these purification methods in removing chlorides from the produced particles was investigated and the final materials were analyzed with various techniques. Three processes were applied for the purification: (a) washed with water (Prec:M_{H2O}) b) washed alternately with water and ethanol (Prec:M_{EtOH}), and c) tempered at 550 °C (Prec:$M_{550°C}$).

The ATR-FT-IR spectra (Figure 3 A) show a slight decreased N–H absorption band (at 1450 cm^{-1}) for samples washed with H_2O or H_2O and EtOH. After tempering the particles, all vibration bands in the range of 4000–900 cm^{-1} disappeared and new bands at 600 and 465 cm^{-1} for the antisymmetric and

Figure 3. (A) ATR-FT-IR spectra and (B) TGA curves of the SnO_2 powders with different post-treatments.

Journal of Inorganic and General Chemistry
ZAAC
Zeitschrift für anorganische und allgemeine Chemie

RESEARCH ARTICLE

symmetric stretching vibrations of Sn-O—Sn groups became visible.[13]

The crystallite sizes obtained from XRD of the washed particles correspond with those of untreated samples. The signal of NH_4Cl at $2\theta = 32.7°$ is no longer observed, implying that the amount of the chloride byproduct after washing is at least below the XRD detection limit (Figure S5 A). While washing procedures with water seem to be successful in the purification, they have one drawback, which is the loss of large amounts of product.

This can be due to the formation of soluble tin hydroxide and oxide hydrate complexes.[75] Hence an alternating washing procedure with water and ethanol might be a better choice. The thermal behavior of the samples was investigated with TGA (Figure 3 B). The mass losses (Δm) of the samples Prec:M_{ap}, Prec:M_{H2O}, Prec:M_{EtOH} and Sol:M_{ap} are 15, 15, 11 and 8%, respectively. For a better insight into the decomposition processes the emerging gases were identified using TGA-FT-IR coupling (Figure 4 and Table S1). Up to high temperatures, gas evolutions were detected and it is obvious that the sample Prec:M_{EtOH}

and the Sol:M_{ap} show high CO_2 signals, contrary to Prec:M_{ap} and Prec:M_{H2O}.

For Prec:M_{ap}, initially the evolution of H_2O is observed, which reaches its maximum at $140°C$ and is present up to $600°C$ (as can also be seen from the temperature-dependent absorption profiles in Figure S6, which were obtained from the 3D FT-IR plots). The release of ammonia starts at $110°C$ and finds a maximum at $180°C$. The signal is present up to $500°C$. At $275°C$ a slight CO_2 evolution starts and from $490°C$ characteristic vibration bands for HCl at $2570–3090\ cm^{-1}$ are visible (Figure S7 A, $530°C$). This observation confirms that chlorides can be (partly) removed from the sample by heating it above $500°C$.[5]

Probably N_2O is formed due to the decomposition of an ammonia derivate. The temperature values for the other samples (Prec:M_{H2O}, Prec:M_{EtOH}, Sol:M_{ap}) are listed in detail in Table S1 and S2. The sample Prec:M_{H2O} shows a similar thermal behavior as the sample Prec:M_{ap}, but the amount of water released in the first TGA step is higher and the amount of NH_3 decreased. The temperature for NH_3 release is also higher,
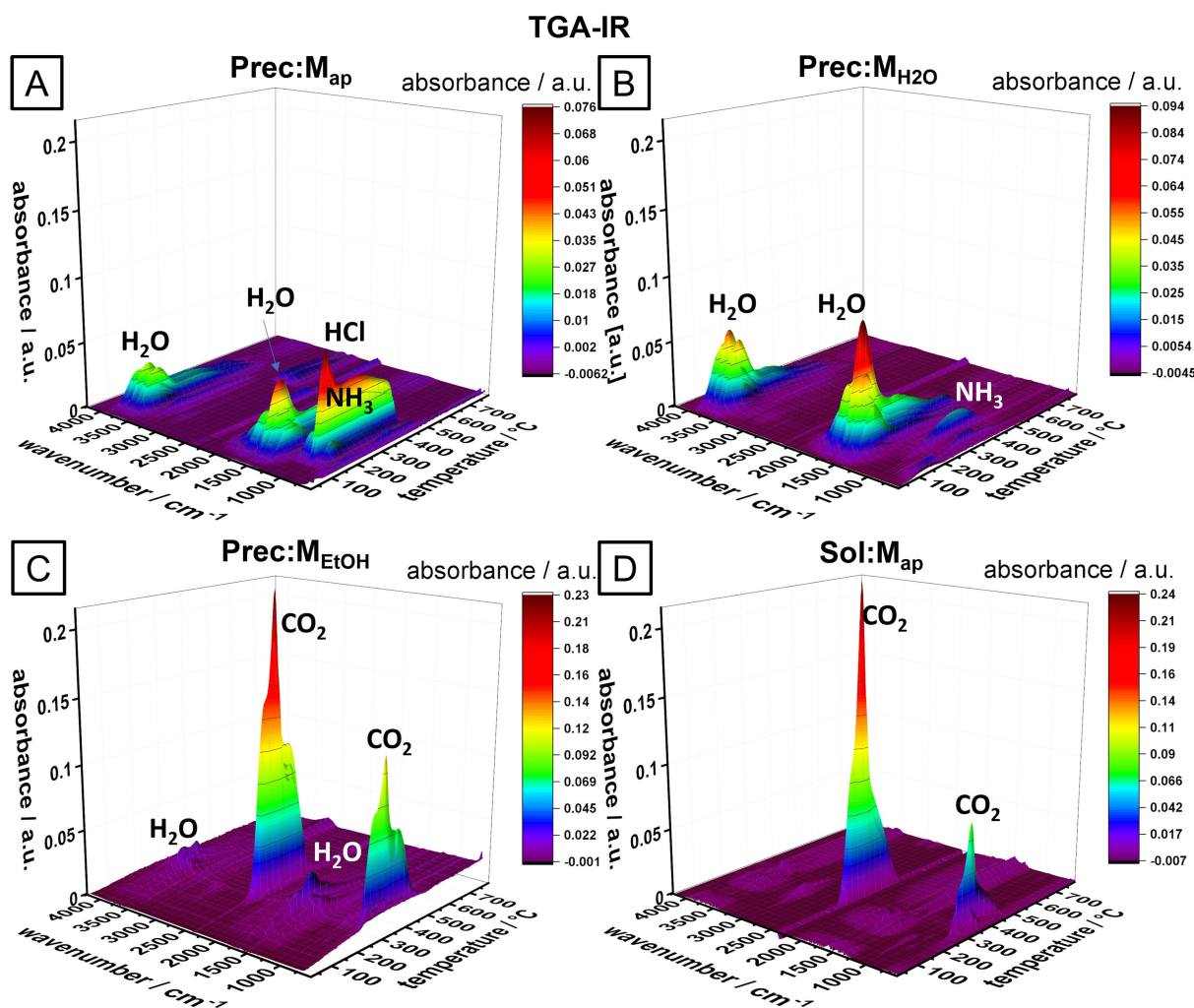

Figure 4. 3D-FT-IR spectra of the SnO_2 samples with different post-treatments. The spectra show the gas emission of the samples during the TGA measurements.

which can be explained by the assumption that Prec:M_{ap} contains a high amount of unbound or weakly bound ammonia (because it has been added in excess), which vaporizes at lower temperatures. Furthermore, no signals of HCl or N_2O were recorded, leading to the assumption that the washing was successful and most of the chloride was removed. The same conclusion can be drawn for the sample Prec:M_{EtOH}. These results were verified by EDX measurements (Table 3): after washing the samples, the values for chlorine were much lower than in the as prepared sample and even lower than those of the unwashed samples after annealing at 550 °C. The TGA curve of the sample Prec:M_{EtOH} differs from the other described samples by a low mass loss in the temperature range 25–200 °C and a strong CO_2 release in the temperature range 230–470 °C. The CO_2 evolution up to these high temperatures indicates chemisorbed EtOH. During the washing steps with EtOH, hydroxy groups undergo an etherification and form Sn-OEt groups. The exchange of the surface groups and the fact that high temperatures are necessary to remove these groups might change the surface reactivity and could play a role for further surface modifications, catalyst activities or low temperature sensor measurements.

The sol-gel sample displays a similar CO_2 evolution as the sample Prec:M_{EtOH}, also in the same temperature range and with a comparable mass loss. Between 200 and 300 °C two additional gases were detected at 2790–3000 cm^{-1} and 3016 cm^{-1}, which could not be clearly identified. The corresponding wavenumber range is characteristic for C–H stretching vibrations of alkyl and alkenyl groups, so that it is likely that the signals originate from decomposition products of *t*-butoxy groups of the educt and the solvent. As expected, no chloride signals were detected in this sample.

Elemental analyses (Table 3) confirmed the results from TGA-IR. A lower nitrogen content was measured in the washed samples than for the as prepared sample. The carbon content of the sample Prec:M_{EtOH} and the sample Sol:M_{ap} were significantly increased.

Whether EtOH is chemisorbed on the particles, as suggested by the TGA-IR studies, can be demonstrated by solid-state NMR measurements.[76] A distinction between chemisorbed and physisorbed molecules is possible by contact time variation in solid-state ^{13}C CP-MAS-NMR studies due to the different mobility of the determined species. In Figure 5 A the spectra of the sample Prec:M_{EtOH} measured in SPE-MAS mode and CP-MAS mode with different contact times are presented. In the SPE-MAS spectrum, where the signal intensity is not enhanced by

abundant hydrogen atoms, two distinct peaks are visible at 15.6 ppm (methyl C) and at 56.6 ppm (methylene C). At a contact time of 6 ms and CP-MAS mode a broad, small signal appears beside each of the original peaks at 17.0 and 59.2 ppm. By further deceasing the contact time the broad signals get more and more dominant, and the sharp signals disappear. The mobility of chemisorbed, covalently bound ethanol is more limited than the mobility of physisorbed ethanol, which is just attached by hydrogen bond. Depending on the mobility, different contact times are necessary to detect certain species. With long contact times (e.g. 6 ms) it is possible to observe mainly signals from hydrogen bonded ethanol, which has a more flexible conformation. The spectra confirm that both, physisorbed and chemisorbed ethanol are present in the ethanol washed sample.

Summarizing the washing experiments, the results showed that the ammonia and chloride content in the '*as prepared*' samples can be significantly reduced by washing the precipitated particles or by heating them to 550 °C. In the case of washing with ethanol, ethoxy groups bind to the SnO_2 surface, which was confirmed by solid-state NMR. Therefore, a release of CO_2 up to 470 °C is visible in the TGA of the washed particles. The same behavior was observed for sol-gel particles prepared in alcoholic solution. The particles washed with water showed no more signals of chloride and only slight signals of ammonia in the TGA-IR measurements. They showed a mass loss of approx. 15 % in the temperature range between 50−485 °C of the TGA curve, which is mainly due to the evaporation of adsorbed water and the condensation of OH groups.

The influence of chlorine contamination on the tempering behavior of the samples was investigated. A comparison of the crystallite size growth and the phase composition at elevated temperatures for SnO_2 samples with and without chloride contaminations (samples Pre:M_{ap} and Pre:M_{H2O}) were performed by in-situ XRD measurements (Figure S5 B and Figure 5 B). The sample Pre:M_{H2O} was measured with an internal standard (30 wt % α-Al_2O_3) in order to improve the height adjustment of the sample during the measurement and to ensure an accurate determination of the SnO_2 reflection position.

The scans display broad reflection bands for SnO_2 at low temperatures, which are characteristic for nanocrystalline materials. With increasing temperature, the reflection bands get sharper and more defined, which is caused by the growth of the crystallites (Figure 5 B and D). The reflection at $2\theta = 43.4°$ is generated by the steel sample holder and is not specific for the samples. A possible amorphous content is low or stays constant

Table 3.
Chemical composition from elemental analysis (C, N) and EDX (Sn, Cl). n. d.: not detectable.

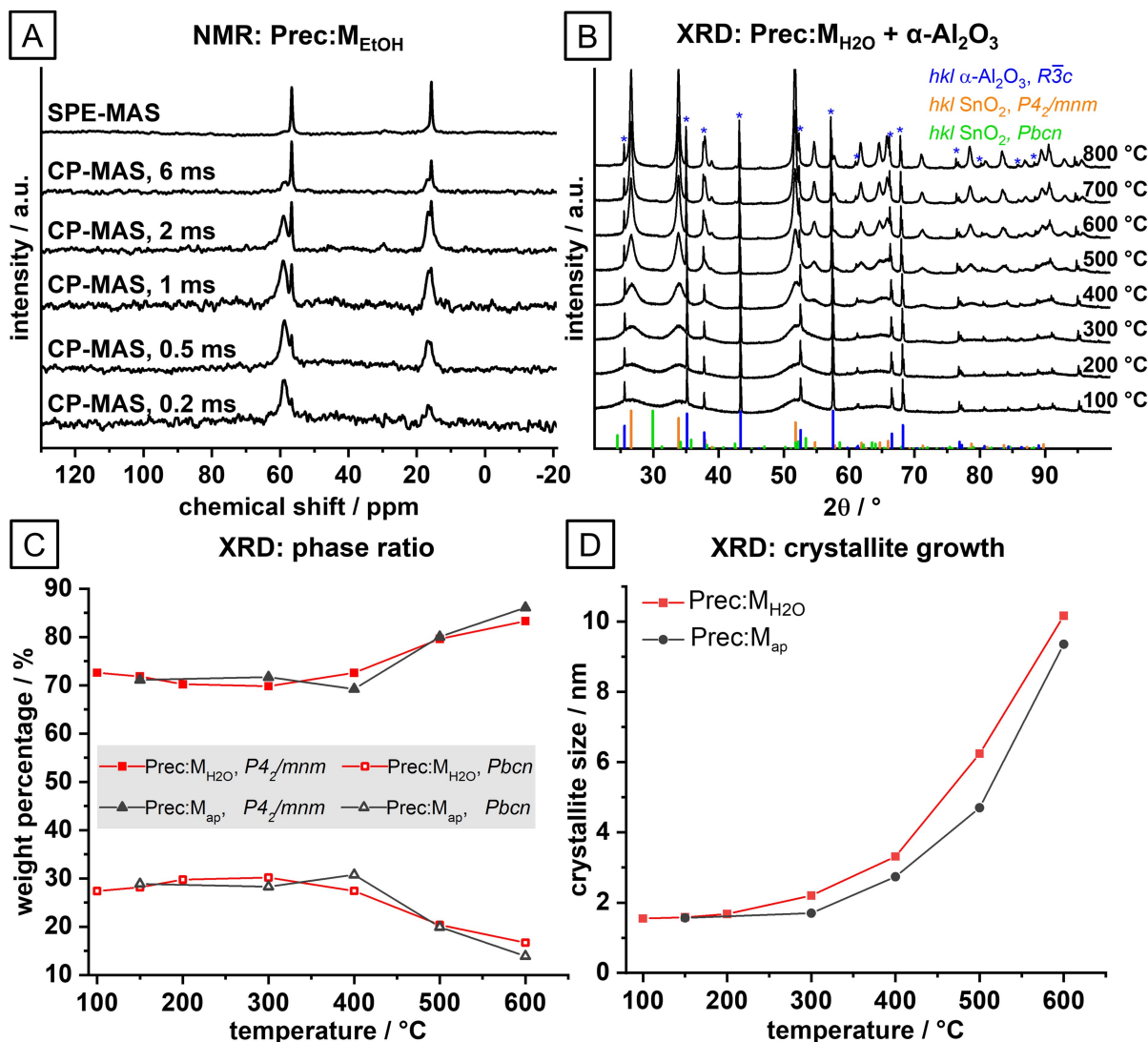|	C wt%	N wt%	Sn wt%	Cl wt%	Cl:Sn atomic ratio
Prec:M_{ap}	0.2	2.0	74.7	4.6	0.2
Prec:M_{H2O}	0.1	0.6	78.4	0.2	0.01
Prec:M_{EtOH}	1.4	0.6	78.1	0.1	0.003
Prec:$M_{550°C}$	n. d.	n. d.	83.3	0.4	0.003
Sol:M_{ap}	0.4	n. d.	79.6	0.6	0.02

Figure 5. (A) SPE- and CP-MAS-NMR spectra of the sample Prec:M_{EtOH} with different contact times (0.2–6.0 ms) and **(B)** *in-situ* XRD scans of the water washed sample (Prec:M_{H2O}) containing an internal standard (Al_2O_3) and assignment of the reflections. **(C)** Phase weight fractions and **(D)** crystallite sizes of the as prepared (Prec:M_{ap}) and water washed (Prec:M_{H2O}) samples at different sintering temperatures obtained from *in-situ* XRD.

during the heat treatment because the refined α-Al_2O_3 content keeps also unchanged. To be sure that a varying amorphous phase is not described by the background function it was only refined by a 4th order polynomial, meaning that an amorphous part should be mainly covered by the less defined, orthorhombic phase. However, an exact quantification of the amorphous phase was not possible. The analysis of the XRD-data revealed that the crystallite size for the rutile phase increases, while the size for the orthorhombic crystallites remains constant or even decreases slightly. During the heat treatment, a reduction of defects takes place, which produces a crystallite growth for the particles in the tetragonal phase. It can be assumed that the orthorhombic crystallites also undergo degradation of defects and growth, which, however, is accompanied by a transformation into the tetragonal structure. In order to achieve a

reliable and consistent monitoring of the changes in the phase fractions, the variable parameters were reduced: The crystallite size of the orthorhombic phase was set to a constant value of 1.6 nm and its lattice parameters were set to literature values.[70] An anisotropic grain size, as observed in the samples of Jensen *et al.*,[70] could not be determined here, which is why isotropic sizes could be used for the evaluations. With these simplifications the behavior of the phase composition was determined exemplary for the sample Pre:M_{H2O} (Figure 5 C). The initial orthorhombic phase fraction of the sample dried at 100 °C, was approx. 27 wt%. When the sample was heated, the content of the PbO_2-type structure increased slightly and reached 30 wt% at 300 °C. After exceeding this temperature, a progressive decrease of this phase was observed. Brito *et al.*[77] described a similar trend. They determined the phase processes of a

monolithic SnO_2 xerogel during a thermal sintering by extended X-ray absorption fine structure (EXAFS) experiments and XRD and found that due to dehydration and oxolation reactions between 110 and 250 °C, an amorphization of the cassiterite structure takes place. Above 250 °C, the condensation reactions of surface OH-groups of adjacent crystallites re-enforce the long-range crystalline order and a progressive crystal growth is observed in the temperature range between 300 and 700 °C. In this study, no indications for amorphization processes could be found. Instead, it is proposed that an initial increase of the *Pbcn* phase in the investigated material is the cause for the decrease of the tetragonal structure in the relevant temperature range.

In order to further investigate the growing behavior, the sample Prec:M_{H2O} was annealed for 5 h at 1200 °C, resulting in pure tetragonal SnO_2 (Prec:M_{1200}). *In-situ* XRD scans were performed from Prec:M_{1200} and Prec:M_{H2O} up to 600 °C. For the sample Prec:M_{1200} the temperature dependence of the lattice parameters (a and c) and the volume (V) were determined as a polynomial of 2nd degree (Equation S1–3). By applying Equation S4 the volume expansion coefficient $\alpha_V = 1.44 \cdot 10^{-5}$ K^{-1} was estimated. From α_V the mean linear expansion coefficient $\alpha_L = 4.80 \cdot 10^{-4}$ K^{-1} was approximated (Equation S5). Analogous $\alpha_a = 4.68 \cdot 10^{-6}$ K^{-1} and $\alpha_c = 4.99 \cdot 10^{-6}$ K^{-1} were determined. These values are slightly smaller than those reported in the literature: $\alpha_a = 4.90 \cdot 10^{-6}$ K^{-1}, $\alpha_c = 5.42 \cdot 10^{-6}$ K^{-1}.[61]

Figure 6 shows the values of V for the sample Prec:M_{H2O} as measured and corrected for thermal expansion using Equation S3. At temperatures of 400 °C and above, Prec:M_{H2O} shows values of V close to the reference. However, at temperatures of 300 °C and below, the unit cell volume is relatively high, primarily due to a prolongation of the a-axis. The studies show

that both, the surface and the crystal lattice of the particles are occupied by OH or Cl.

Figure 5 D describes the crystal growing during heat treatment for the precipitation samples with and without water washing. At temperatures below 200 °C only a slow crystallite growth occurs, whereas in the temperature range from 200–600 °C the rate is increased. Both samples start from almost the same initial crystallite size (1.6 nm).

During the thermal treatment, an increased growth is observed for the sample Pre:M_{H2O}, resulting in a crystallite size of 6.2 nm at 500 °C, while the crystallites of sample Prec:M_{ap} have an average size of 4.7 nm at this temperature. At a temperature of 600 °C, the crystallite sizes approach each other again (10.2 and 9.4 nm for Prec:M_{ap} and Pre:M_{H2O}) This initial slower growth of the Prec:M_{ap} sample could be due to the covering of the surface with chloride, which is degraded at higher temperatures.

Microjet SnO_2 Material in Sensor Application

As part of a preliminary study, we investigated the potential use of the synthesized particles as ethanol gas sensors. For this purpose, sol-gel derived particles from the continuous route were suspended in ethanol and applied to a gas sensor substrate consisting of a 3×3 mm² ceramic plate (alumina) with platinum planar heater and platinum electrodes. The particles were annealed at 400 °C for 2 hours prior to the measurements with ethanol gas. At the same time, a commercial sensor (GGS 1330, UST Umweltsensortechnik GmbH, Geratal, Germany) was tested as a reference under identical experimental conditions.
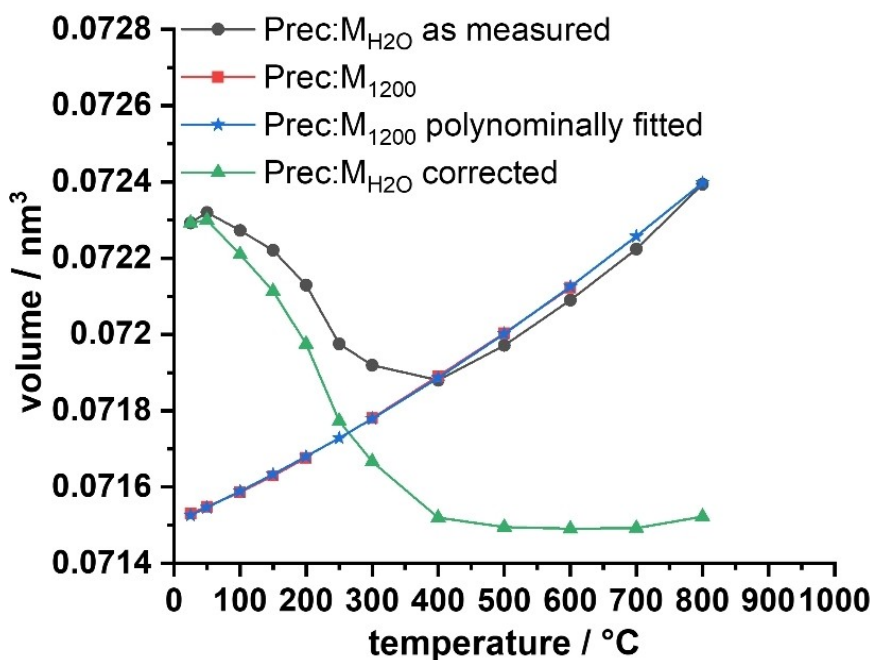

Figure 6. Temperature dependence of the unit cell volume of the sample Prec:M_{H2O} as measured (grey) and corrected (green). The thermal expansion was obtained from the fit function (blue) of the sample Prec:M_{1200} (red).

The measurements were performed at 400 °C, with a gas flow of 80 ml/min and the ethanol concentration was varied between 10, 20 and 40 ppm (Figure 7 A).

The response (G/G_0) of both sensors increased with higher ethanol concentration, while the Sol:M_{ap} sample showed better values compared to the reference (Figure 7 B). This test confirms that continuous routes can be used for the fabrication of SnO$_2$ nanomaterials. The suspensions derived from the microjet can be directly applied in sensor applications and show a similar behavior in ethanol sensing like industrial sensors. This means without purification and further treatment we succeeded in the large-scale production of similar materials used in optimized sensor applications.

Conclusion

In summary, ultrafine SnO$_2$ nanoparticles were successfully prepared using both a discontinuous and a continuous method by precipitation and sol-gel reactions. The resulting materials showed particle and crystallite sizes between 1.7–3.0 nm and between 1.7–2.3 nm, respectively, with the sizes of the sol-gel particles being slightly larger than those from the precipitations. XRD measurements showed that the particles consist of a tetragonal main phase ($P4_2/mnm$) and an orthorhombic high-pressure phase (HP2, $Pbcn$). The synthesis methods proved to be robust to external influences and allowed a seamless transition from batch to continuous processing, maintaining consistent concentrations and temperatures and obtaining particles with similar properties. Different cleaning methods to remove salt impurities were investigated. Washing with water and alternate washing with water and ethanol significantly decreased the chloride content in the samples. However,

washing with water resulted in high yield losses due to the formation of soluble tin species and the use of ethanol introduced ethoxy groups on the particle surfaces. Thermal treatment (550 °C for 2 h) required the least technical effort but resulted in a crystallite growth. The sample Prec:M_{H2O} showed an increased growth, reaching 6.2 nm at 500 °C, while Prec:M_{ap} only grew to 4.7 nm. At 600 °C, their sizes converge to 10.2 nm and 9.4 nm, respectively. The slower initial growth of Prec:M_{ap} may be due to surface chloride coverage, which degrades at higher temperatures. XRD studies revealed that both the surface and the crystal lattice of the particles are occupied by OH or Cl. This led to a high initial volume of the $P4_2/mnm$ unit cell, especially due to the elongation in the direction of the a-axis. During heating, the volume decreased significantly and approached literature values from about 400 °C.

These results illustrate the efficiency and side effects of the different chloride removal methods. The potential application of these SnO$_2$ nanoparticles as ethanol gas sensors was validated, showing a sensitivity comparable to commercial sensors immediately after production, without any additional treatment.

Experimental Section

Materials

Tin(IV) chloride pentahydrate (98%) and tin(IV) chloride, anhydrous (99%) were purchased from ChemPur, aqueous ammonia (25%) was obtained from VWR International GmbH. Diethylamine (>99%) and t–butanol (>99%) were purchased from Merck and Grüssing GmbH. All chemicals were used as received.
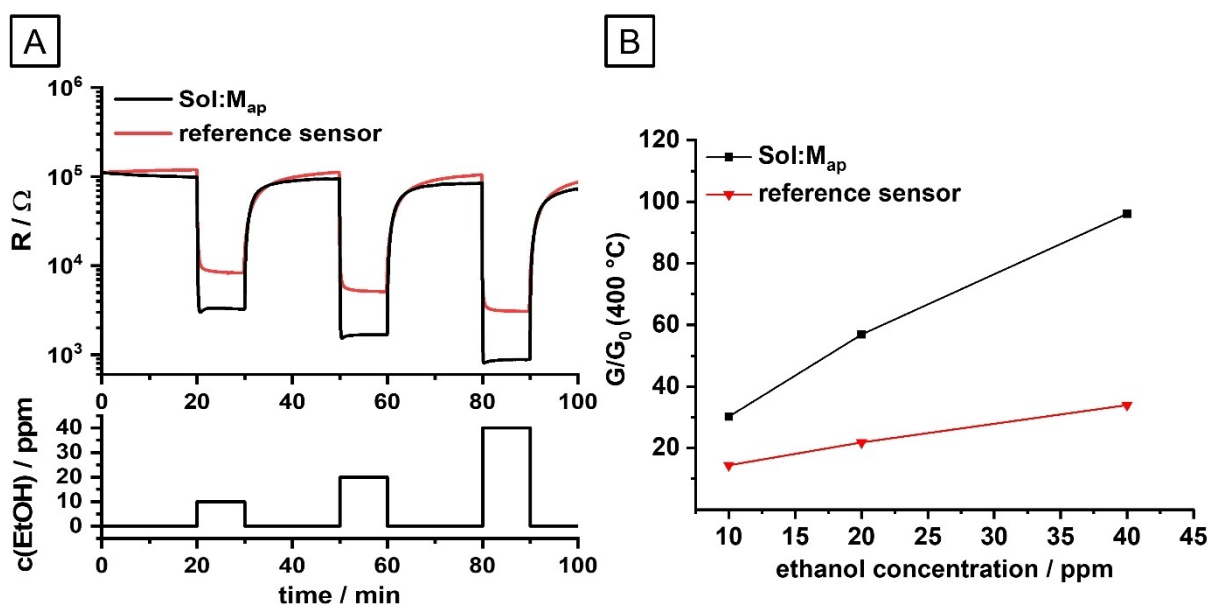

Figure 7. A) Ethanol sensing test of the sample Sol:M_{ap} and a commercial reference sensor (GGS 1330, UST) for 10, 20 and 40 ppm ethanol. **B)** Sensor response for different ethanol concentrations.

Precursor preparation: synthesis of Sn(O^{t}Bu)$_4$

The precursor synthesis was carried out according to the methods described by Thomas[78] and Chandler et al.[79] The synthesis was performed under argon atmosphere applying Schlenk techniques. In a three-necked, round bottom flask equipped with a reflux condenser, dropping funnel and magnetic stir bar, 9 ml (76.1 mmol, 1.0 eq.) anhydrous SnCl$_4$ were dissolved in 150 ml dry n-heptane and cooled to 15 °C. A solution of 34 ml (330 mmol, 4.3 eq.) diethylamine in 30 ml n-heptane were added dropwise and the mixture was stirred for 10 min at RT. After adding 26.56 g (358 mmol, 4.7 eq.) t–butanol, a white precipitate was formed. To retain an extensive mixing the solution was diluted by adding 60 ml of n-heptane and was stirred overnight ($\approx$17 h) at RT. The precipitate was vacuum filtered and washed three times with 20 ml of cold n-heptane. The filtrate dried under reduced pressure and a pale-yellow solid was obtained. The compound was purified by distillation/ sublimation at 41–43 °C (0.03 mbar) and 20.3 g (65 %) of a colorless, crystalline solid were obtained. ^{1}H NMR (400 MHz, C$_6$D$_6$, 20 °C): δ = 1.46 (s, 12×CH$_3$) ppm; ^{119}Sn NMR (149 MHz, C$_6$D$_6$, 20 °C): δ = $-$372.2 ppm; ^{13}C{^{1}H} NMR (101 MHz, C$_6$D$_6$, 20 °C): δ = 75.0 ($^2J_{Sn-C}$ = 23 Hz, 4 x C(CH$_3$)$_3$), 34.1 ($^3J_{Sn-C}$ = 14 Hz, 12 x CH$_3$) ppm (Figure S1–S3).

Apparatus

Microjet-Reactor

The Microjet reactor setup (Scheme 1 A) was described in various previous studies[50–51,80–81]. In detail it consists of two HPLC pumps (LaPrep P110 preparative HPLC pumps, VWR), which transport the precursor solutions with high pressure ($\approx$30–40 bar) to the mixing chamber. The reagent solutions enter the reactor (MicroJet reactor, Synthesechemie Dr. Penth GmbH, Heusweiler, Germany) from opposing sides through micro nozzles (300 µm) and collide there as impinging jets. After mixing, the product suspension is directly removed from the reactor by a nitrogen gas stream (8 bar), which hits the colliding jets at an angle of 90°.

The outlet tube (stainless steel) is 1.5 mm in diameter and had a length of 90 cm. The particle suspension was collected in a polyethylene or glass vessel. The desired reaction temperature was adjusted by placing the MicroJet reactor in a tempered water bath.
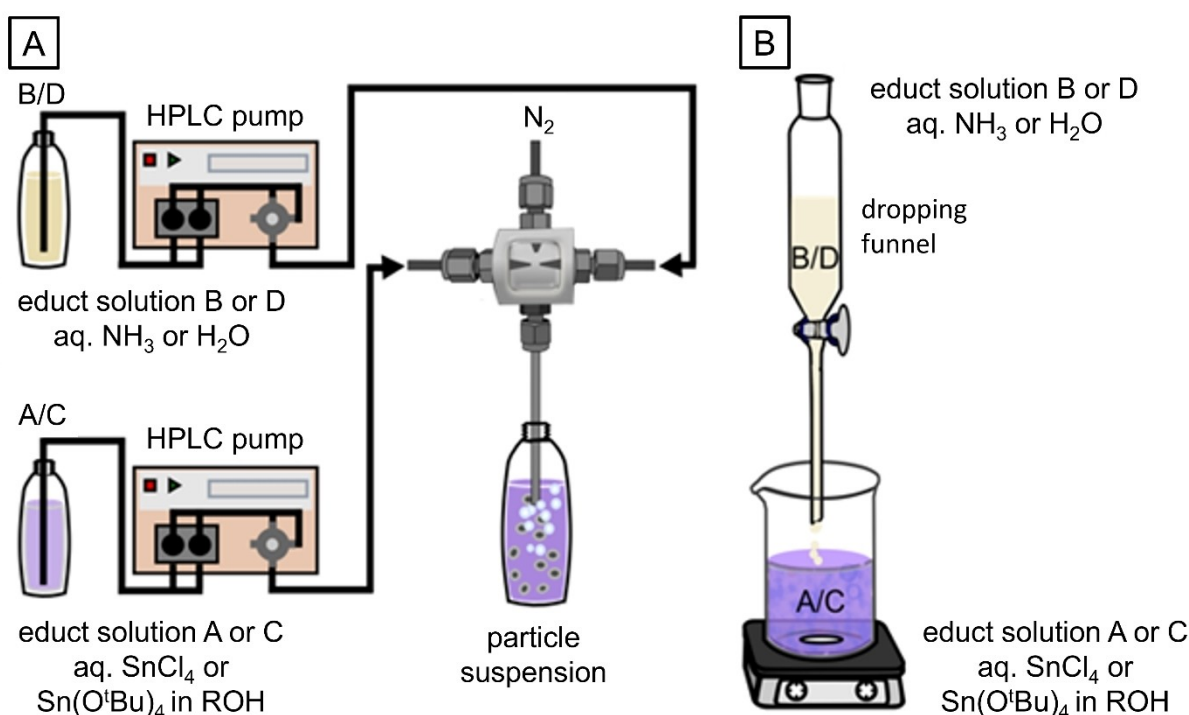
Beaker Synthesis

The batch synthesis was accomplished in a glass beaker (250 ml) placed on a hot plate stirrer with temperature sensor and dropping funnel (Scheme 1 B).

Preparation of Nanoparticles

Synthesis

For the precipitation reactions, an aqueous solution of tin(IV) chloride pentahydrate (0.1 M) (solution A) and an aqueous solution of ammonia (2 M) (solution B) were prepared. For the sol-gel reaction a solution of the tin(IV) t-butoxide (0.1 M) in t-butanol (solution C) and deionized water (solution D) were used. All experiments were carried out at 70 °C. In the beaker syntheses 80 ml of solution B or D were added dropwise to 80 ml of solution A or C within a time interval of 15 min and afterwards stirred for another 5 minutes. In the Microjet reactor process the reagent solutions A and B (for samples from tin chloride) or C and D (for samples from tin alkoxide) were fed into the system with a flow rate of 250 ml/min. Precursor solutions with t-butanol (T$_m$ $\approx$ 26 °C) as solvent were warmed to 30 °C prior the reaction to liquefy the medium. The precursor solution C was stored under argon and pumped directly from the Schlenk flask into the system.

Scheme 1. Set-up for SnO$_2$ nanoparticles preparation by A) Microjet reactor technique, B) beaker synthesis.

Post-Treatment

The particles were isolated from suspension by centrifugation (8000 rpm, 7012 g, 10 min). A part of these particles was a) separated, b) washed with water (ca. 5×25 ml) and c) tempered at 550 °C for 2 h. Particles from a second microreactor synthesis (same conditions as before) were d) washed alternating with ethanol and water (ca. 5×25 ml). All samples were dried separately at 100 °C. The particles were obtained as white or pale-yellow powders.

Characterization Methods

Solution NMR spectra were recorded with an Avance III HD 400 spectrometer (Bruker, Billerica, USA) at 20 °C in C_6D_6 (^1H at 400 MHz, ^{13}C at 101 MHz, ^{119}Sn at 149 MHz). The signals were referenced to solvent chemical shifts (for H and C) or to the device parameters (for Sn).

Solid-state NMR spectroscopy in single pulse excitation or cross-polarization and magic-angle spinning mode (SPE-MAS- and CP-MAS-NMR) were measured on an AV400WB spectrometer (Bruker, Billerica, USA). The samples were packed in zirconia rotors, which were spun at 13 kHz under nitrogen. The ^{13}C NMR spectra were recorded at a frequency of 100.7 MHz and a recycle delay of 10 s (SPE-MAS-NMR) or 3 s (CP-MAS-NMR). The contact time in the CP-MAS experiments was varied between 0.2 and 6 ms. Adamantane served as external standard.

Attenuated total reflectance Fourier transform infrared (ATR FT-IR) spectra were obtained on a Vertex 70 spectrometer (Bruker Optics, Ettlingen, Germany). Prior each sample measurement a reference spectrum was recorded. Then, the dried powders were scanned under ambient air. Each spectrum contains 64 scans with a resolution of 4 cm^{-1} in a wave number range of 500–4200 cm^{-1}. The spectra were normalized to provide a better comparability.

Thermogravimetric analysis (TGA) were performed on a TG 209 F1 Iris (Netzsch, Gerätebau GmbH, Selb, Germany). The dried samples were filled in alumina crucibles and heated with 20 K/min from RT to 800 °C under synthetic air (10 ml/min O_2, 40 ml/min N_2).

For **TGA-FT-IR** analyses the TGA device was connected with the Vertex 70 IR spectrometer (Bruker Optics, Ettlingen, Germany). The dried samples (≈ 50 mg) were filled in alumina crucibles and heated with 20 K/min from RT to 800 °C under synthetic air (10 ml/min O_2, 40 ml/min N_2). The evolving gases were transferred through a heated line (200 °C) to the IR spectrometer. The FT-IR spectra were recorded with 32 scans, a resolution of 4 cm^{-1} and in a range of 4500 to 600 cm^{-1}.

Powder X-ray diffraction was carried out with a D8-A25-Advance diffractometer (Bruker AXS, Karlsruhe, Germany) in Bragg-Brentano θ-θ-geometry (goniometer radius 280 mm) with Cu-K$_\alpha$-radiation ($\lambda_{\alpha 1} = 154.0596$ pm) and a 192-channel LYNXEYE detector. XRD patterns were recorded in a 2θ range from 7 to 130° with a step size of 0.013° and a total scan time of one or two hours. For *in-situ* measurements at elevated temperatures the heating chamber XRK 900 (Anton Paar GmbH, Graz, Austria) was used. The samples were heated with 20 K/min and kept at constant temperatures during the individual scans. Prior each measurement the temperature was equilibrated for at least 10 min. For the sample Prec:M$_{ap}$ and Prec:M$_{1200}$ XRD patterns in the temperature range of 25–600 °C were recorded with a 2θ range of 7–110° and a measuring time of one or two hours. For the sample Prec:M$_{H2O}$ a temperature range of 25–800 °C was used and a 2θ range of 10–130°. The measuring time was two hours. For all samples a step size of 0.013° was applied.

The program TOPAS V5[82] was applied for the Rietveld refinements. The background was fitted by a Chebychev polynomial function of 15th degree (standard measurements) or 4th degree (measurements at elevated temperatures), the fluorescence induced background was reduced by discriminating the detector. The structure and microstructure refinements were accomplished by the help of crystal structure data from the inorganic crystal structure database (ICSD)[83]. Instrumental line broadening was empirically determined by LaB$_6$ as a reference material and taken into account for evaluation of the other scans using the fundamental parameters approach.[84]

Transmission electron microscopy (TEM) was carried out using a JEM-2010 microscope (JEOL, Akishima, Japan). The samples were suspended in ethanol or water, supported by an ultrasound treatment (10 min). The suspension (ca. 30 μL) was applied dropwise on Plano S160–3 copper grids. Unless otherwise stated, the size distributions of the particles were determined by measure the diameter of at least 50 individual particles with the image analysis software ImageJ.[85] **High-resolution TEM** (HR-TEM) images and **selected area electron diffraction** (SAED) patterns were acquired using a JEM–F200 microscope (JEOL, Akishima, Japan) equipped with a thermal field-emission source.

Energy-dispersive X-ray spectroscopy (EDX) was carried out with a Genesis 2000 spectrometer (EDAX, Mahwah, USA) attached to the chamber of a JSM-7000-F scanning electron microscope (JEOL, Akishima, Japan). A voltage of 20 kV was applied.

Elemental analyses were performed with a Vario Micro Cube (Elementar, Langenselbold, Germany).

Sensor Measurements and Characterization

Sensor Coating

The prepared SnO_2 particles were dispersed in ethanol (ethanol : SnO_2 5:1, by mass) using an ultrasonic bath. A layer of this dispersion was applied onto a sensor substrate (3×3 mm^2 alumina plate) with platinum planar heater (Umweltsensortechnik GmbH, Geratal, Germany) by drop casting (15×0.4 μl). After each drop, the ethanol was allowed to evaporate. The coating was annealed at 400 °C for 2 hours using the two heating pins of the sensor substrate.

Sensor Measurements

The experiment was carried out using a gas mixing apparatus, as described in detail in previous publications.[86] A zero air generator supplied 80 ml/min dry carrier gas, into which ethanol from a gas cylinder was injected to achieve concentrations of 10 ppm, 20 ppm, and 40 ppm, each for a duration of 10 minutes. During the measurement period, the sensor was maintained at a constant temperature of 400 °C.

Acknowledgements

Conflicts of Interests

There are no conflicts to declare.

Data Availability Statement

The data that support the findings of this study are available in the supplementary material of this article.

[1] W. Göpel, K. D. Schierbaum, *Sens. Actuators, B* **1995**, *26*, 1–12.

[2] S. Das, V. Jayaraman, *Prog. Mater. Sci.* **2014**, *66*, 112–255.

[3] X. Hou, Y. Hu, H. Jiang, J. Huo, Y. Li, C. Li, *J. Mater. Chem. A* **2013**, *1*, 13814–13820.

[4] C. S. Maheswari, C. Shanmugapriya, K. Revathy, A. Lalitha, *J. Nanostruct. Chem.* **2017**, *7*, 283–291.

[5] P. Siciliano, *Sens. Actuators, B* **2000**, *70*, 153–164.

[6] L. Feng, Z. Xuan, S. Ji, W. Min, H. Zhao, H. Gao, *Int. J. Electrochem. Sci.* **2015**, *10*, 2370–2376.

[7] N. Barsan, M. Schweizer-Berberich, W. Göpel, *Fresenius J. Anal. Chem.* **1999**, *365*, 287–304.

[8] B. J. Wang, S. Y. Ma, *Vacuum* **2020**, *177*, 109428.

[9] M. Sabarilakshmi, K. Janaki, *J. Mater. Sci. - Mater. Electron.* **2017**, *28*, 8101–8107.

[10] T. Ahmad, S. Khatoon, K. Coolahan, *J. Am. Ceram. Soc.* **2016**, *99*, 1207–1211.

[11] A. Klinbumrung, T. Thongtem, A. Phuruangrat, S. Thongtem, *Jpn. J. Appl. Phys.* **2016**, *55*, 1–7.

[12] T. A. N. Peiris, H. C. Weerasinghe, M. Sharma, J.-E. Kim, M. Michalska, N. Chandrasekaran, D. C. Senevirathna, H. Li, A. S. R. Chesman, D. Vak, J. J. Jasieniak, *Chem. Mater.* **2022**, *34*, 5535–5545.

[13] D. N. Srivastava, S. Chappel, O. Palchik, A. Zaban, A. Gedanken, *Langmuir* **2002**, *18*, 4160–4164.

[14] W. B. Soltan, S. Nasri, M. S. Lassoued, S. Ammar, *J. Mater. Sci. - Mater. Electron.* **2017**, *28*, 6649–6656.

[15] X. Xiang, D. Zhu, D. Wang, *J. Mater. Sci. - Mater. Electron.* **2016**, *27*, 7425–7432.

[16] G. Liu, W.-J. Sun, S.-S. Tang, S.-Q. Liang, J. Liu, *Trans. Nonferrous Met. Soc. China* **2015**, *25*, 3651–3656.

[17] G. Neri, A. Bonavita, G. Micali, G. Rizzo, N. Pinna, M. Niederberger, J. Ba, *Sens. Actuators, B* **2008**, *130*, 222–230.

[18] M. Aziz, S. Saber Abbas, W. R. Wan Baharom, *Mater. Lett.* **2013**, *91*, 31–34.

[19] S. Bhuvana, H. B. Ramalingam, K. Vadivel, E. Ranjith Kumar, A. I. Ayesh, *J. Magn. Magn. Mater.* **2016**, *419*, 429–434.

[20] F. I. Shaikh, L. P. Chikhale, I. S. Mulla, S. S. Suryavanshi, *Ceram. Int.* **2017**, *43*, 10307–10315.

[21] R. Dujardin, F. Delorme, B. Pintault, P. Belleville, C. Autret, I. Monot-Laffez, F. Giovannelli, *Mater. Lett.* **2017**, *187*, 151–153.

[22] J. A. Toledo-Antonio, R. Gutiérrez-Baez, P. J. Sebastian, A. Vázquez, *J. Solid State Chem.* **2003**, *174*, 241–248.

[23] J. Wang, W. Wu, W.-H. Wang, M. Bao, *Ceram. Int.* **2017**, *43*, 4702–4705.

[24] J. X. Zhou, M. S. Zhang, J. M. Hong, J. L. Fang, Z. Yin, *Appl. Phys. A* **2005**, *81*, 177–182.

[25] J. Zhang, L. Gao, *J. Solid State Chem.* **2004**, *177*, 1425–1430.

[26] G. Kelp, T. Tätte, S. Pikker, H. Mändar, A. G. Rozhin, P. Rauwel, A. S. Vanetsev, A. Gerst, M. Merisalu, U. Mäeorg, *Nanoscale* **2016**, *8*, 7056–7067.

[27] P. Jaumier, B. Jousscaume, M. Lahcini, F. Ribotc, C. Sanchez, *Chem. Commun.* **1998**, 369–370.

[28] H. Elhamzaoui, B. Jousseaume, H. Riague, T. Toupance, P. Dieudonné, C. Zakri, M. Maugey, H. Allouchi, *J. Am. Chem. Soc.* **2004**, *126*, 8130–8131.

[29] K. C. Molloy, *J. Chem. Res.* **2008**, *2008*, 549–554.

[30] N. Lecerf, S. Mathur, H. Shen, M. Veith, S. Hüfner, *Scripta Mater.* **2001**, *44*, 2157–2160.

[31] M. Veith, N. Lecerf, S. Mathur, H. Shen, S. Hüfner, *Chem. Mater.* **1999**, *11*, 3103–3112.

[32] M. Veith, J. Lee, M. M. Miro, C. K. Akkan, C. Dufloux, O. C. Aktas, *Chem. Soc. Rev.* **2012**, *41*, 5117–5130.

[33] S. A. Khan, A. Günther, M. A. Schmidt, K. F. Jensen, *Langmuir* **2004**, *20*, 8604–8611.

[34] N. Jongen, M. Donnet, P. Bowen, J. Lemaître, H. Hofmann, R. Schenk, C. Hofmann, M. Aoun-Habbache, S. Guillemet-Fritsch, J. Sarrias, A. Rousset, M. Viviani, M. T. Buscaglia, V. Buscaglia, P. Nanni, A. Testino, J. R. Herguijuela, *Chem. Eng. Technol.* **2003**, *26*, 303–305.

[35] B. Gutmann, D. Cantillo, C. O. Kappe, *Angew. Chem. Int. Ed.* **2015**, *54*, 6688–6728.

[36] Z. Fang, H. Assaaoudi, R. I. L. Guthrie, J. A. Kozinski, I. S. Butler, *J. Am. Chem. Soc.* **2007**, *90*, 2367–2371.

[37] H. L. Hellstern, J. Becker, P. Hald, M. Bremholm, A. Mamakhel, B. B. Iversen, *Ind. Eng. Chem. Res.* **2015**, *54*, 8500–8508.

[38] G.-W. Chu, Q.-H. Zeng, Z.-G. Shen, H.-K. Zou, J.-F. Chen, *Chem. Eng. J.* **2014**, *253*, 78–83.

[39] A. Mamakhel, M. Søndergaard, K. Borup, B. Brummerstedt Iversen, *J. Supercrit. Fluids* **2020**, *166*, 1–8.

[40] M. NaderiNasrabadi, Y. Mortazavi, A. A. Khodadadi, *Sens. Actuators, B* **2016**, *230*, 130–139.

[41] J. Liu, F. Gu, Y. Hu, C. Li, *J. Phys. Chem. C* **2010**, *114*, 5867–5870.

[42] S. D. Bakrania, C. Perez, M. S. Wooldridge, *Proc. Combust. Inst.* **2007**, *31*, 1797–1804.

[43] Y. J. Hong, M. Y. Son, Y. C. Kang, *Adv. Mater.* **2013**, *25*, 2279–2283.

[44] I.-S. Hwang, S.-J. Kim, J.-K. Choi, J. Choi, H. Ji, G.-T. Kim, G. Cao, J.-H. Lee, *Sens. Actuators, B* **2010**, *148*, 595–600.

[45] M. Akram, A. Z. Alshemary, F. K. Butt, Y.-F. Goh, W. A. W. Ibrahim, R. Hussain, *Mater. Lett.* **2015**, *160*, 146–149.

[46] J. Hiemer, A. Clausing, T. Schwarz, K. Stöwe, *Chem. Eng. Technol.* **2019**, *42*, 2018–2027.

[47] M. Periyasamy, A. Saha, S. Sain, M. Mandal, U. Sengupta, A. Kar, *J. Environ. Chem. Eng.* **2020**, *8*, 104604.

[48] A. Betke, G. Kickelbick, *Inorganics* **2014**, *2*, 1–15.

[49] F. P. Lohmann-Richters, C. Odenwald, G. Kickelbick, B. Abel, Á. Varga, *RSC Adv.* **2018**, *8*, 21806–21815.

[50] C. Odenwald, G. Kickelbick, *J. Sol-Gel Sci. Technol.* **2018**, *89*, 343–353.

[51] M. A. Mohamed, S. Arnold, O. Janka, A. Quade, V. Presser, G. Kickelbick, *ChemSusChem* **2023**, *16*, e202202213.

[52] A. V. Nikam, B. L. V. Prasad, A. A. Kulkarni, *CrystEngComm* **2018**, *20*, 5091–5107.

[53] C. A. Ibarguen, A. Mosquera, R. Parra, M. S. Castro, J. E. Rodríguez-Páez, *Mater. Chem. Phys.* **2007**, *101*, 433–440.

[54] G. S. Devi, S. K. Masthan, M. Shakuntala, V. J. Rao, *J. Mater. Sci. - Mater. El.* **1999**, *10*, 545–549.

[55] R. G. Pavelko, A. A. Vasiliev, E. Llobet, X. Vilanova, N. Barrabés, F. Medina, V. G. Sevastyanov, *Sens. Actuators, B* **2009**, *137*, 637–643.

[56] D. Chen, L. Gao, *J. Colloid Interface Sci.* **2004**, *279*, 137–142.

[57] L. Xi, D. Qian, X. Tang, C. Chen, *Mater. Chem. Phys.* **2008**, *108*, 232–236.

[58] S. Fujihara, T. Maeda, H. Ohgi, E. Hosono, H. Imai, S.-H. Kim, *Langmuir* **2004**, *20*, 6476–6481.

[59] H.-C. Chiu, C.-S. Yeh, *J. Phys. Chem. C* **2007**, *111*, 7256–7259.

[60] P. G. Harrison, A. Guest, *J. Chem. Soc., Faraday Trans.* **1987**, *83*, 3383–3397.

[61] J.-J. Zhu, J.-M. Zhu, X.-H. Liao, J.-L. Fang, M.-G. Zhou, H.-Y. Chen, *Mater. Lett.* **2002**, *53*, 12–19.

[62] D. Amalric-Popescu, F. Bozon-Verduraz, *Catal. Today* **2001**, *70*, 139–154.

[63] H. A. Ory, *Anal. Chem.* **1960**, *32*, 509–511.

[64] S. Tazikeh, A. Akbari, A. Talebi, E. Talebi, *Mater. Sci.-Pol.* **2014**, *32*, 98–101.

[65] T. Sakurai, T. Takizawa, *High Temp. - High Press.* **1971**, *3*, 325–331.

[66] J. Haines, J. Léger, *Phys. Rev. B: Condens. Matter.* **1997**, *55*, 11144.

[67] S. R. Shieh, A. Kubo, T. S. Duffy, V. B. Prakapenka, G. Shen, *Phys. Rev. B: Condens. Matter.* **2006**, *73*, 014105.

[68] S. Ono, K. Funakoshi, A. Nozawa, T. Kikegawa, *J. Appl. Phys.* **2005**, *97*, 073523.

[69] S. Ono, E. Ito, T. Katsura, A. Yoneda, M. Walter, S. Urakawa, W. Utsumi, K. Funakoshi, *Phys. Chem. Miner.* **2000**, *27*, 618–622.

[70] K. M. Ø. Jensen, M. Christensen, P. Juhas, C. Tyrsted, E. D. Bøjesen, N. Lock, S. J. L. Billinge, B. B. Iversen, *J. Am. Chem. Soc.* **2012**, *134*, 6785–6792.

[71] G. Bartlett, I. Langmuir, *J. Am. Chem. Soc.* **1921**, *43*, 84–91.

[72] A. Gaber, M. A. Abdel-Rahim, A. Y. Abdel-Latief, M. N. Abdel-Salam, *Int. J. Electrochem. Sci.* **2014**, *9*, 81–95.

[73] Z. Wu, Y. Wang, Y. Zhang, W. Zhang, Q. Liu, Q. Liu, Q. Chen, Y. Li, J. Li, D. He, *Org. Electron.* **2019**, *73*, 7–12.

[74] S. Hatamie, V. Dhas, B. Kale, I. Mulla, S. Kale, *Mater. Sci. Eng., C* **2009**, *29*, 847–850.

[75] A. V. Sidorak, V. V. Ivanov, A. A. Shubin, *Mater. Sci. Appl.* **2011**, *02*, 1219–1224.

[76] S. Pilkenton, D. Raftery, *Solid State Nucl. Magn. Reson.* **2003**, *24*, 236–253.

[77] G. E. S. Brito, V. Briois, S. H. Pulcinelli, C. V. Santilli, *J. Sol-Gel Sci. Technol.* **1997**, *8*, 269–274.

[78] I. M. Thomas, Owens-Illinois, Inc.: Method for producing stannic tertiary alkoxide, US 3,946,056, **1974**, 1–7.

[79] C. D. Chandler, G. D. Fallon, A. J. Koplick, B. O. West, *Aust. J. Chem.* **1987**, *40*, 1427–1439.

[80] B. Krüner, C. Odenwald, A. Tolosa, A. Schreiber, M. Aslan, G. Kickelbick, V. Presser, *Sustain. Energy Fuels* **2017**, *1*, 1588–1600.

[81] M. Abdirahman Mohamed, S. Arnold, O. Janka, A. Quade, J. Schmauch, V. Presser, G. Kickelbick, *J. Mater. Chem. A* **2023**, *11*, 19936–19954.

[82] Topas 5, Bruker AXS, Karlsruhe, Germany **2014**.

[83] G. Bergerhoff, I. D. Brown, in *Crystallographic databases*, F. H. Allen et al., Chester, International Union of Crystallography, **1987**.

[84] R. W. Cheary, A. A. Coelho, J. P. Cline, *J. Res. Natl. Inst. Stand. Technol.* **2004**, *109*, 1–25.

[85] C. A. Schneider, W. S. Rasband, K. W. Eliceiri, *Nat. Methods* **2012**, *9*, 671–675.

[86] N. Helwig, M. Schüler, C. Bur, A. Schütze, T. Sauerwald, *Meas. Sci. Technol.* **2014**, *25*, 055903.